Geomechanics and Engineering, *Vol. 40, No. 4 (2025) 295-305*
https://doi.org/10.12989/gae.2025.40.4.295

Elastic wave propagation and attenuation characteristics of roof fracture source

Peng-Fei Zhang[1,2,3], Tong-Bin Zhao*[1,2,3], Xu-Fei Gong[1,2,3], Yan Tan[1,2,3] and Chuan-Qing Guo[4]

[1]*College of Energy and Mining Engineering, Shandong University of Science and Technology, Qingdao 266590, China*
[2]*State Key Laboratory of Mining Disaster Prevention and Control Co-founded by Shandong Province and the Ministry of Science and Technology, Shandong University of Science and Technology, Qingdao 266590, China*
[3]*Shandong Key Laboratory of Intelligent Prevention and Control of Dynamic Disaster in Deep Mines, Shandong University of Science and Technology, Qingdao 266590, China*
[4]*Energy Group Co., Ltd., Jining No.2 Coal Mine ,Jining 272012, China*

(*Received November 16, 2022, Revised December 30, 2024, Accepted January 6, 2025*)

Abstract. The propagation attenuation law of elastic waves generated by rock mass fractures in strata is of great significance in explaining engineering problems, such as rock bursts. In this study, a wave velocity model was established based on the actual stratum conditions of the Jining No.2 coal mine in China. The propagation process of different types of elastic waves is simulated using the elastic wave equation and finite difference method. The attenuation coefficients of various elastic wave parameters propagating at different positions were calculated. Based on the calculated results, an attenuation equation for the elastic wave energy is proposed. The results show that the propagation of S-waves and P-waves in strata is similar to each other, and wave pattern transformation occurs at the interface of the strata. The magmatic rocks played a role in channeling and reflecting elastic wave propagation, leading to the occurrence of low-energy aftershocks in the coal seams. The peak displacement, peak stress, and energy density of the elastic wave that propagated to the coal seam after the siltstone layer fracture of the roof of the 3_{down} coal seam decreased to 28%, 25%, and 9% of the source, respectively. The attenuation of elastic wave energy is highly correlated with the propagation distance, and the attenuation equation can be represented as an exponential function. These results are of great significance for revealing the propagation attenuation process of elastic waves in the stratum.

Keywords: elastic wave; energy attenuation; propagation characteristics; rock burst; roof fracture

1. Introduction

During coal mining, elastic waves generated by roof failure propagate along the strata as described by Czarny *et al*. (2021), Li *et al*. (2019), Christensen (1971). Fan *et al*. (2021), He *et al*. (2016), Zhao *et al*. (2018) found that when the elastic wave propagates to the surrounding rock of the roadway, rock bursts may be induced. Therefore, the propagation law of elastic waves in strata is of great significance in describing the mechanism of rock bursts.

Nonlinear attenuation in elastic wave propagation has long been a topic of common concern for overseas and domestic scholars. According to the elastic wave theory as described by Gegenhuber (2016) and Lak *et al*. (2018), a series of wave phenomena occur during the propagation of elastic waves, including geometric diffusion, reflection, scattering, transmission, wave pattern conversion, and attenuation according to Zhu *et al.* (2020), Fu *et al.* (2020), Huang *et al.* (2022). These phenomena gradually reduce the elastic wave, affecting the propagation of energy from the source to a specific location (such as a coal seam).

Numerical simulations are the most effective method for studying this type of problem. Domestic and foreign scholars such as Perino *et al.* (2010), Fan *et al.* (2022), Lak *et al*. (2019), Zeng *et al.* (2022) have studied the propagation characteristics of elastic waves in coal rock mass through numerical simulation. Chong *et al.* (2020), Berjamin *et al.* (2018), Han and Dai (2018) analyzed the influences of media type; Lei and Sornette (2021), Li and Tao (2015), Tao *et al.* (2016) the stress environment; Zhu *et al.* (2020), Gallagher *et al.* (2022) the damage degree; Sebastian and Sithram (2018), Babanouri and Fattahi (2018), Rioyos-Romero *et al.* (2022) the joint distribution; Shen *et al.* (2022) and Cheng *et al.* (2021) the microstructure and other factors on the propagation attenuation of elastic waves. However, most existing research focuses on the influence of various factors on the elastic wave propagation process. Few studies have been conducted on the propagation attenuation of elastic waves generated by different vibration sources in the strata.

Based on this, a wave velocity field model was established based on the actual stratum conditions of the Jining No. 2 coal mine in China. The elastic wave equation and the finite difference method were used to simulate and calculate the propagation process of different types of elastic waves in the stratum. The entire calculation process

*Corresponding author, Professor
E-mail: ztbwh2001@126.com

ISSN: 2005-307X (Print), 2092-6219 (Online)

was realized using C language programming. The attenuation coefficients of displacement, stress, and energy when the elastic wave propagates to different positions were calculated, and the influence of the elastic wave generated by the roof fracture on the coal seam was obtained. Finally, the influence of different focal locations on the attenuation coefficient of elastic waves is discussed, and an attenuation equation of elastic wave energy is proposed based on the calculated results. These results are of great significance for revealing the propagation attenuation process of elastic waves in the stratum.

2. Numerical calculation method

2.1 Elastic wave equation

The elastic wave equation is the basic law of elastic wave propagation in a stratum. It can calculate the wave field formed by the vibration propagating from a certain position to any position in the stratum and then obtain the distribution of displacement, stress, and energy in the stratum space. The basic form of the elastic wave equation is given by Eq. (1)

$$\begin{cases} \dfrac{\partial^2 u}{\partial t^2} = V_P^{\,2}\left(\dfrac{\partial^2 u}{\partial x^2}+\dfrac{\partial^2 v}{\partial x\partial y}+\dfrac{\partial^2 w}{\partial x\partial z}\right)+V_S^{\,2}\left(\dfrac{\partial^2 u}{\partial y^2}+\dfrac{\partial^2 u}{\partial z^2}-\dfrac{\partial^2 v}{\partial x\partial y}-\dfrac{\partial^2 w}{\partial x\partial z}\right) \\ \dfrac{\partial^2 v}{\partial t^2} = V_P^{\,2}\left(\dfrac{\partial^2 u}{\partial x\partial y}+\dfrac{\partial^2 v}{\partial y^2}+\dfrac{\partial^2 w}{\partial y\partial z}\right)+V_S^{\,2}\left(\dfrac{\partial^2 v}{\partial x^2}+\dfrac{\partial^2 v}{\partial z^2}-\dfrac{\partial^2 u}{\partial x\partial y}-\dfrac{\partial^2 w}{\partial y\partial z}\right) \\ \dfrac{\partial^2 w}{\partial t^2} = V_P^{\,2}\left(\dfrac{\partial^2 u}{\partial x\partial z}+\dfrac{\partial^2 v}{\partial y\partial z}+\dfrac{\partial^2 w}{\partial z^2}\right)+V_S^{\,2}\left(\dfrac{\partial^2 w}{\partial x^2}+\dfrac{\partial^2 w}{\partial y^2}-\dfrac{\partial^2 u}{\partial x\partial z}-\dfrac{\partial^2 v}{\partial y\partial z}\right) \end{cases} \tag{1}$$

where V_P and V_S are the propagation velocities of P- and S-waves, respectively, in the formation medium. u, v, and w are the particle vibration displacements and $\boldsymbol{u} = ui_x + vi_y + wi_z$ is the displacement vector of the particle.

In this equation, the vibration displacement of the particle can be directly obtained. Furthermore, the stress can be obtained from the displacement field using Eq. (2)

$$\begin{cases} \sigma_x = c_{11}\dfrac{\partial u}{\partial x}+c_{12}\dfrac{\partial v}{\partial y}+c_{13}\dfrac{\partial w}{\partial z} \\ \sigma_y = c_{21}\dfrac{\partial u}{\partial x}+c_{22}\dfrac{\partial v}{\partial y}+c_{23}\dfrac{\partial w}{\partial z} \\ \sigma_z = c_{31}\dfrac{\partial u}{\partial x}+c_{32}\dfrac{\partial v}{\partial y}+c_{33}\dfrac{\partial w}{\partial z} \\ \tau_{yz} = c_{44}\left(\dfrac{\partial w}{\partial y}+\dfrac{\partial v}{\partial z}\right) \\ \tau_{xz} = c_{55}\left(\dfrac{\partial w}{\partial x}+\dfrac{\partial u}{\partial z}\right) \\ \tau_{xy} = c_{44}\left(\dfrac{\partial v}{\partial x}+\dfrac{\partial u}{\partial y}\right) \end{cases} \tag{2}$$

where c_{ij} is the coefficient of stiffness, and the relation between the density of the medium and the velocity of the P- and S-waves is

$$\begin{cases} c_{11} = c_{22} = c_{33} = \rho V_P^2 \\ c_{12} = c_{13} = c_{23} = \rho V_P^2 - 2\rho V_S^2 \\ c_{44} = c_{55} = c_{66} = \rho V_S^2 \end{cases} \tag{3}$$

In addition, the energy field is the focus of this study. Energy density and energy flux density were used to describe the energy required for the propagation of elastic waves. The energy density can be obtained from the displacement field according to Eq. (4).

$$E = \frac{1}{2}\rho\left(\frac{\partial \mathbf{u}}{\partial t}\right)^2 \tag{4}$$

The energy flow density vector can be obtained from the displacement and stress, according to Eq. (5)

$$\mathbf{K} = \begin{bmatrix} \sigma_x & \tau_{xy} & \tau_{xz} \\ \tau_{xy} & \sigma_y & \tau_{yz} \\ \tau_{xz} & \tau_{yz} & \sigma_z \end{bmatrix} \cdot \begin{bmatrix} \dfrac{\partial u}{\partial t} \\ \dfrac{\partial v}{\partial t} \\ \dfrac{\partial w}{\partial t} \end{bmatrix} \tag{5}$$

In the process of calculation, Take K's mold $|\mathbf{K}|$ as energy parameters.

2.2 Rock fracture pattern

The rock in the stratum breaks up and forms a vibration source, and an inelastic deformation zone is formed in the adjacent area, outside of which only elastic waves propagate. The equal-potency model is typically used to approximate the seismic source, which ignores the nonlinear deformation of the source region and corresponds to its linear wave equation. Specifically, the displacement generated by the equivalent force on the seismic source point is consistent with that generated by the real force acting on the seismic source location. During the fracture process of the working face roof, the force exerted on the rock medium causes the deformation (including elastic and inelastic deformations). The displacement generated by this force is expressed in the spherical coordinates r,θ,and ϕ, as shown in Eq. (6)

$$\begin{cases} u^P = \dfrac{1}{4\pi\rho v_p^{\,3} r} R^P(M_{ij}) \\ u^{SV} = \dfrac{1}{4\pi\rho v_s^{\,3} r} R^{SV}(M_{ij}) \\ u^{SH} = \dfrac{1}{4\pi\rho v_s^{\,3} r} R^{SH}(M_{ij}) \end{cases} \tag{6}$$

(1) Tensile seismic source

After mining the coal seam, the roof strata were bent and deformed. When the span of the rock strata reaches a certain length, tensile failure easily occurs in the middle of the rock beam (Guo *et al*. 2022, Zhao *et al*. 2020), forming a tensile seismic source. The tensile seismic source can be equivalent to a pair of symmetric tensions in the horizontal direction, and the displacement field generated by breaking is expressed by Eq. (7). The radiation patterns of P-wave and S-waves are shown in Fig. 1.

$$\begin{cases} u_r = \dfrac{1}{4\pi\rho v_p^{\,3} r}\sin^2\theta\cos^2\varphi M_{11} \\ u_\Theta = \dfrac{1}{8\pi\rho v_s^{\,3} r}\sin 2\theta\cos^2\varphi M_{11} \\ u_\varphi = -\dfrac{1}{8\pi\rho v_s^{\,3} r}\sin\theta\sin 2\varphi M_{11} \end{cases} \tag{7}$$

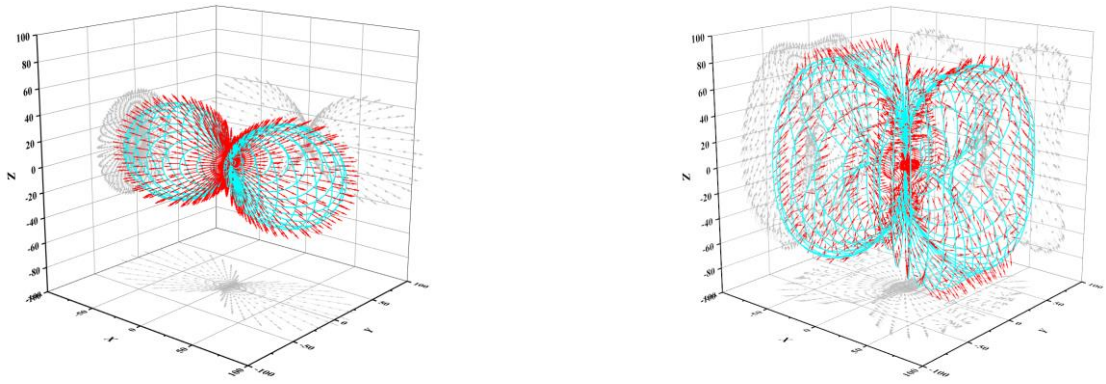

(a) P-wave (b) S-wave

Fig. 1 Tensile source radiation wavefield

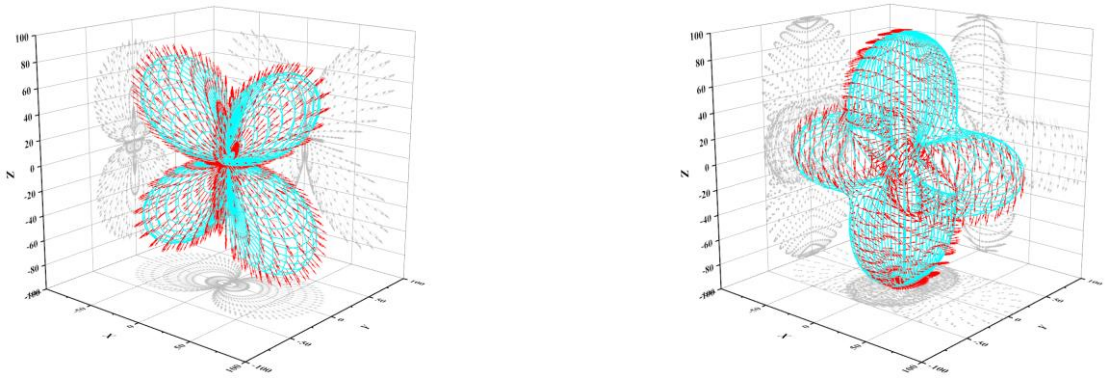

(a) P-wave (b) S-wave

Fig. 2 Shear source radiation wavefield

(2) Shear seismic source

When there are geological structures, such as faults around the roof of the working face, under the influence of uneven subsidence of strata, motion in the form of shear slip may occur, forming a shear seismic source (Zhao *et al*. 2016). The shear seismic source is equivalent to the action of a pair of shear forces. The displacement field generated by the fracture is expressed by Eq. (8). The radiation patterns of P-wave and S-waves are shown in Fig. 2.

$$\begin{cases} u_r = \dfrac{1}{4\pi\rho v_p^{\ 3} r}\sin 2\theta\cos\varphi M_{13} \\ u_\Theta = \dfrac{1}{4\pi\rho v_S^{\ 3} r}\cos 2\theta\cos\varphi M_{13} \\ u_\varphi = -\dfrac{1}{4\pi\rho v_s^{\ 3} r}\cos\theta\sin\varphi M_{13} \end{cases} \tag{8}$$

According to the above method of equal effect analysis, the displacement expression of the equivalent seismic source can be obtained and further combined with the actual physical and mechanical parameters of the roof, and the propagation attenuation characteristics of the roof fracture energy source can be quantitatively evaluated.

3. Construction of numerical model

3.1 Engineering prototype

In this study, the No. 10 mining area of the Jining No. 2 Coal Mine was used as the prototype. The No. 10 mining area is located in the middle of the coalfield, east of the Balipu fault protection coal pillar, west of the 39464000-longitude line, south of the northern boundary of the No.11 mining area, and north of the Yanxin railway coal pillar. The main production coal seam in this area is a 3_{down} coal seam with a dip angle of 3°–12°, an elevation of -620–-850 m, and a ground elevation of +33.70 to +38.58 m. The stratigraphic lithology and its characteristics are shown in Fig. 3.

The structural morphology of the coal seam in the No.10 mining area is high in the northwest and southwest and low in the middle. The Baizhuang anticline southeast of the mining area and the Xuzhuang syncline north of the mining area are the main geological structures in this area. There are three major faults in the mining area: the Balipu fault (H = 170–260 m) in the east, the F103 fault (H = 0–8 m) and the F274 fault (H = 0–16 m) in the middle.

3.2 Construction of wave velocity field model

For the numerical solution of the elastic wave equation described in Section 2.1, a variety of numerical methods can be used including the finite element, finite difference, discrete element, pseudo-spectral, and spectral element methods. Considering the complexity, calculation accuracy, and calculation efficiency of the actual formation structure,

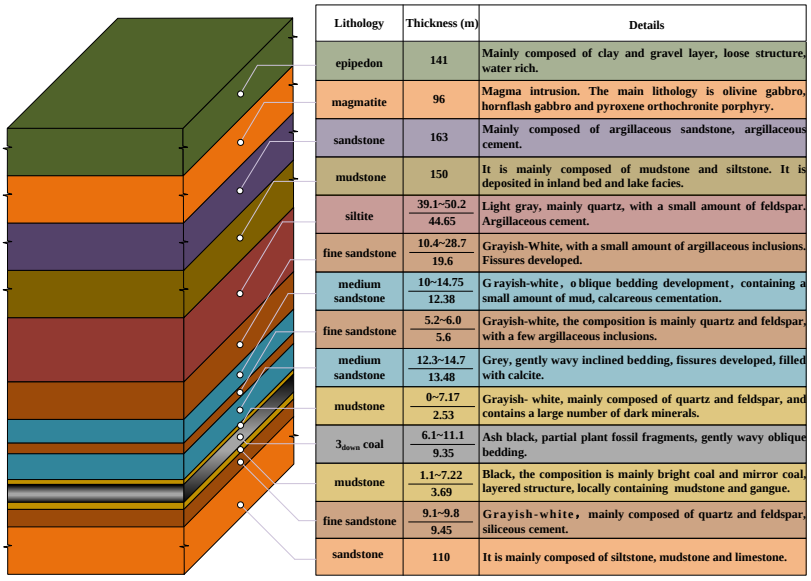

Lithology	Thickness (m)	Details
epipedon	141	Mainly composed of clay and gravel layer, loose structure, water rich.
magmatite	96	Magma intrusion. The main lithology is olivine gabbro, hornflash gabbro and pyroxene orthochronite porphyry.
sandstone	163	Mainly composed of argillaceous sandstone, argillaceous cement.
mudstone	150	It is mainly composed of mudstone and siltstone. It is deposited in inland bed and lake facies.
siltite	39.1~50.2 / 44.65	Light gray, mainly quartz, with a small amount of feldspar. Argillaceous cement.
fine sandstone	10.4~28.7 / 19.6	Grayish-White, with a small amount of argillaceous inclusions. Fissures developed.
medium sandstone	10~14.75 / 12.38	Grayish-white, oblique bedding development, containing a small amount of mud, calcareous cementation.
fine sandstone	5.2~6.0 / 5.6	Grayish-white, the composition is mainly quartz and feldspar, with a few argillaceous inclusions.
medium sandstone	12.3~14.7 / 13.48	Grey, gently wavy inclined bedding, fissures developed, filled with calcite.
mudstone	0~7.17 / 2.53	Grayish- white, mainly composed of quartz and feldspar, and contains a large number of dark minerals.
3_{down} coal	6.1~11.1 / 9.35	Ash black, partial plant fossil fragments, gently wavy oblique bedding.
mudstone	1.1~7.22 / 3.69	Black, the composition is mainly bright coal and mirror coal, layered structure, locally containing mudstone and gangue.
fine sandstone	9.1~9.8 / 9.45	Grayish-white, mainly composed of quartz and feldspar, siliceous cement.
sandstone	110	It is mainly composed of siltstone, mudstone and limestone.

Fig. 3 Stratigraphic comprehensive histogram

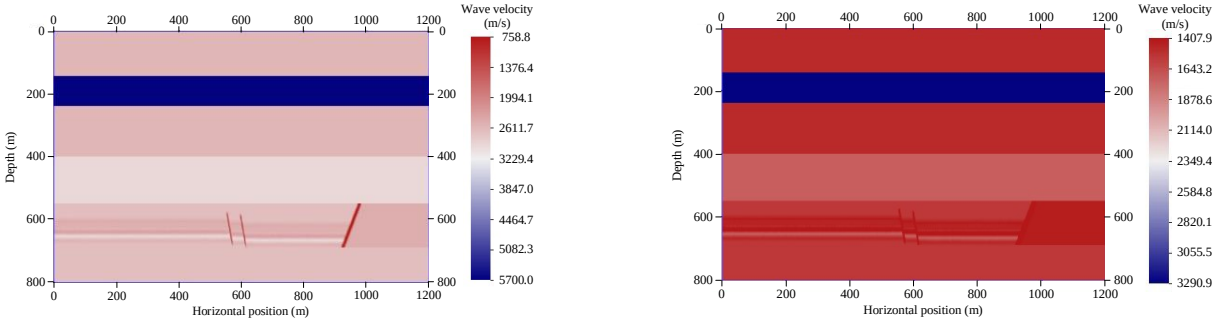

(a) Velocity field of P-wave (b) Velocity field of S-wave

Fig. 4 Numerical model of formation wave velocity field at $103_{down}03$ working face

the finite-difference method was used in this study. The basic principle is to divide the stratum calculation area into regular grids and define the medium parameters and wave-field quantities at each grid point. Using the source wave field as the input, elastic wave equation programming in C language was used to compute the parameter response at each grid point.

To simulate the propagation attenuation process of elastic waves caused by the roof fracture of the $103_{down}03$ working face, the formation wave velocity field model was established. The model was a two-dimensional plane model with dimensions of 1200×800 m. The spacing between the discrete grids was longitudinal dz = 2 m and transverse dx = 2 m. The discrete sampling interval was set as dt = 0.2 ms. After demarcating the range of the model, the formation parameters were converted into the velocity of P-wave and S-wave, among which the velocity fields of P-wave and S-wave are shown in Fig. 4. The input coordinates of the source are (800, 380), and the specific location is in the siltstone layer, approximately 60 m above the coal seam.

3.3 Wave field characteristics

According to the analysis of roof fracture modes in Section 2.2, the two types of limiting forms of the elastic wave field induced by roof fracture are pure P-wave and S-wave sources. Figs. 5 and 6 shows the elastic wave snapshots of the P-wave source and S-wave source in the numerical simulation. The propagation process of the two types of elastic waves is shown through the vertical component of node displacement.

(1) The P-wave initially arrives at the 3_{down} coal seam when T = 150, whereas the S-wave initially arrives at the 3_{down} coal seam when T = 250. The propagation velocity of the S-wave source is lower than that of the p-wave, which is determined by the properties of the rock medium in the stratum. Because the stratum is anisotropic, the two types of elastic waves are converted into another wave pattern in the process of propagation; thus, the wave field characteristics generated by the two types of sources have a certain similarity.

(2) Because there is a 100 m thick magmatic rock layer at a depth of 150–250 m in the strata, its vertical and horizontal wave propagation velocities are significantly higher than those of the surrounding rock layer. As a result, it becomes a “waveguide layer,” that is, the elastic wave produces significant reflection at the interface between the magmatic rock and adjacent rock strata. After the seismic displacement caused by the roof fracture source propagates

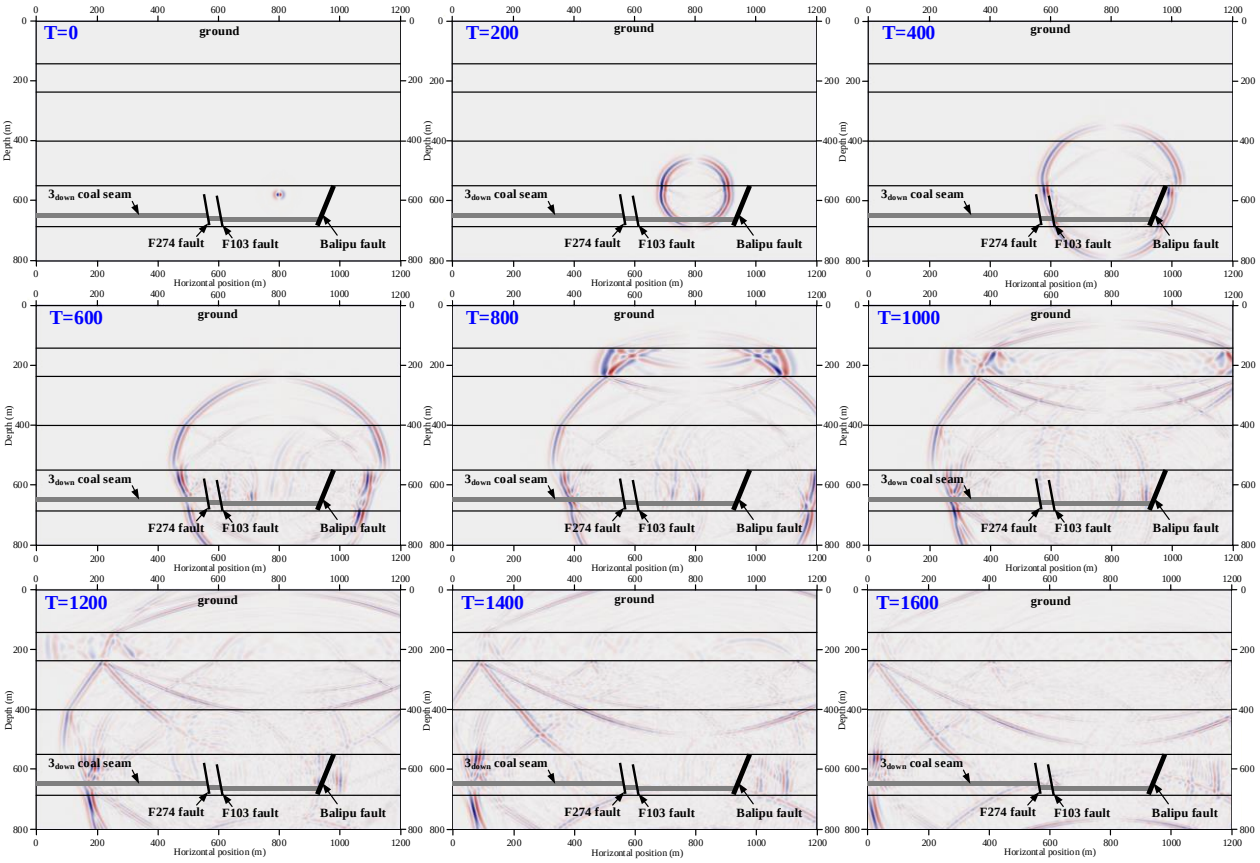

Fig. 5 P-wave wavefield snapshot

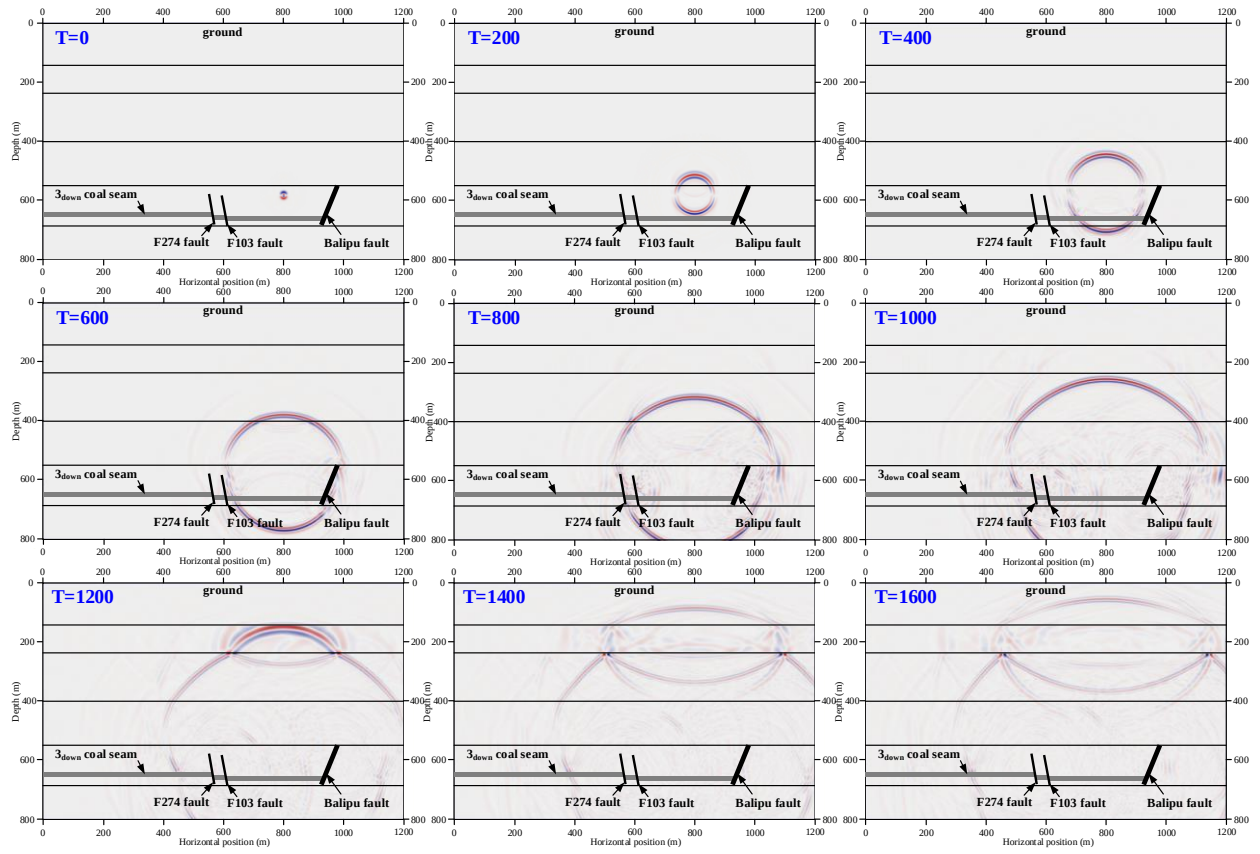

Fig. 6 S-wave wavefield snapshot

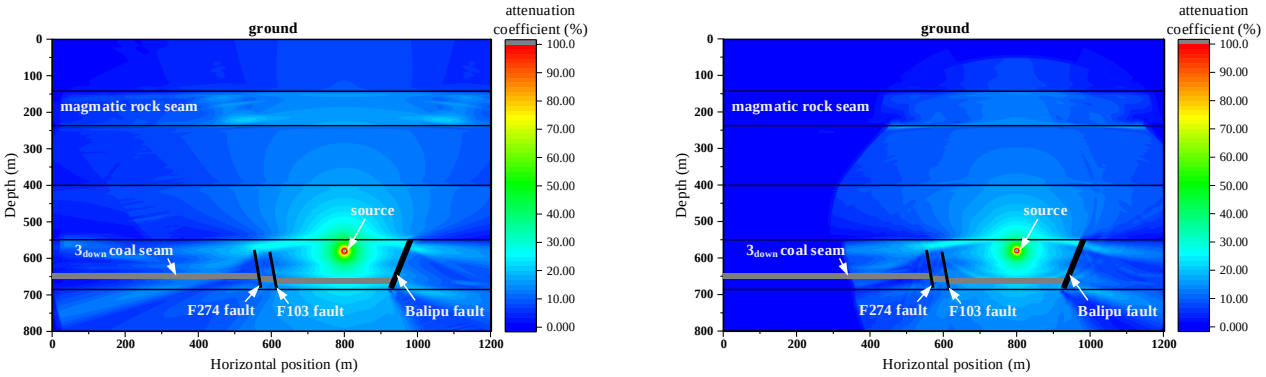

(a) Displacement field of the P-wave (b) Displacement field of the S-wave

Fig. 7 Displacement attenuation coefficient distribution cloud map

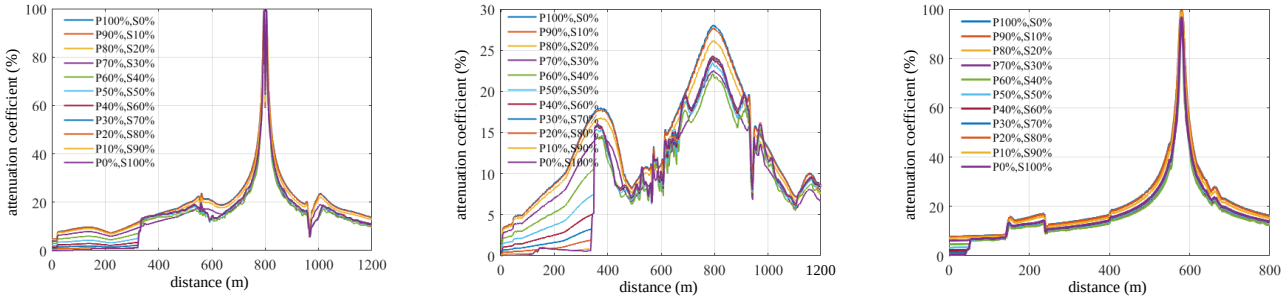

(a) z = 580 (b) z = 650 (c) x = 800

Fig. 8 Displacement attenuation coefficient evolution curve

upward to the magmatic rock layer, part of the elastic wave displacement is reflected and then propagates downward to the coal seam, resulting in the occurrence of aftershocks in the coal seam. The energy of the aftershocks was lower than that of the initial shocks. At the same time, more displacement components were retained in the magmatic rocks and rapidly spread horizontally along the magmatic strata. This effect reduces the transmission of source energy to the surface and plays the role of an energy diversion.

(3) Wave pattern conversion occurred at the interface of all strata. After the P-wave propagates to the interface, it generates not only the transmission and reflection of the P-wave but also the S-wave. S-waves also produce P-waves when they reach an interface. Owing to the different propagation speeds of the longitudinal and transverse waves, this conversion action continuously "breaks up" the elastic wave energy, which gradually spreads to the 3_{down} coal seam.

(4) When the elastic wave propagates to the vicinity of the fault, there is an obvious "divergence" phenomenon in the wave front, which is due to the scattering of the wave field caused by the local low speed of the fault plane and the drastic change in the surrounding medium, which further disperses the elastic wave energy.

In conclusion, the actual structural morphology, and physical and mechanical properties of the overlying rock on the $103_{down}03$ working face play an important role in channeling and dispersing the roof fracture energy. This dispersion effect is superimposed with the geometric diffusion effect of elastic wave propagation, which causes a small part of the energy released by the roof fracture to gradually propagate to the 3_{down} coal seam. Therefore, the propagation attenuation behavior of elastic waves must be quantitatively analyzed.

4. Attenuation law of elastic wave parameters

4.1 Displacement attenuation law

The types of elastic waves generated by different roof fractures are different, and their attenuation laws may also differ. In practice, roof fractures are very complicated. However, regardless of the type of fracture, the generated elastic wave can be decomposed into P-waves and S-waves. Therefore, by changing the amplitude ratio of P-wave and S-waves in the source, all roof fracture types can be covered. To analyze the attenuation characteristics of the elastic wave displacement, the peak displacement value at the source was taken as the reference value, and the grid point displacement value in the entire space was normalized to obtain the attenuation coefficient of displacement. The calculation formula is shown in Eq. (9)

$$\gamma_{ui} = \frac{u_i}{u_s} \tag{9}$$

where i is the number of grid points in the space, γ_{ui} the displacement attenuation coefficient at point i, u_i the displacement value at point i, and u_s the displacement value at the source.

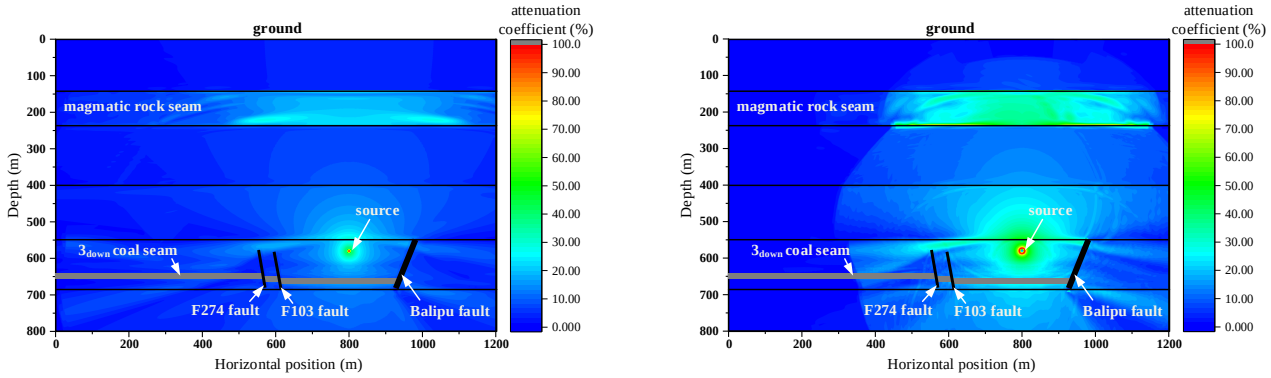

(a) Principal stress field of P-wave (b) Principal stress field of S-wave

Fig. 9 Stress attenuation coefficient distribution cloud map

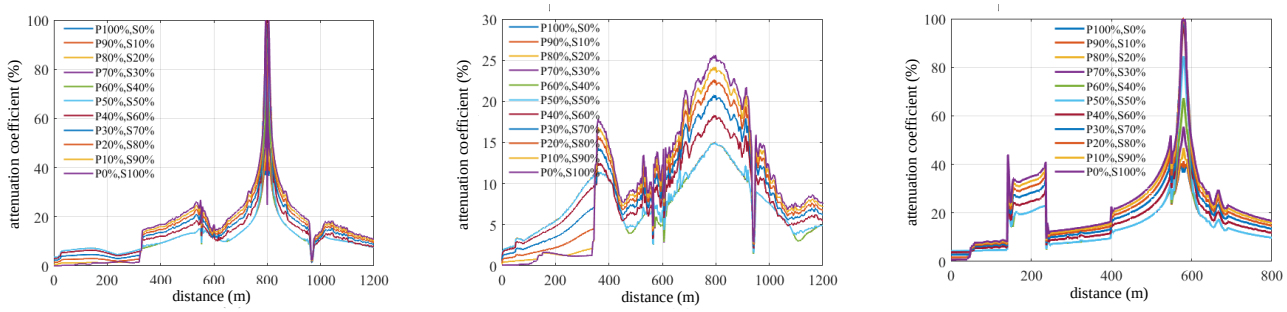

(a) z = 580 (b) z = 650 (c) x = 800

Fig.10 Stress attenuation coefficient evolution curve

Fig. 7 shows the distribution of the displacement attenuation coefficients of P-wave and S-waves. At the same time, three measuring lines were arranged at x = 800 m, z = 580 m, and z = 650 m in the model, and the displacement attenuation coefficient of the grid points on the measuring line was calculated. The distribution curve of the attenuation coefficient is shown in Fig. 8.

(1) At the same source elevation (z = 580 m), the displacement attenuation coefficient has a roughly normal distribution. The elastic wave displacement issued by the source decreased rapidly to both sides, the attenuation coefficient within 200 m rapidly decreases to 20%, and the attenuation speed outside 200 m gradually decreases. The elastic wave displacement at the boundary of the model decreased to approximately 10% of the source.

(2) The elastic wave propagated to the coal seam (z = 650 m), and the peak displacement attenuation was less than 28% of the source. The attenuation coefficient within 300 m in the coal seam directly below the source was approximately linearly distributed, and the peak displacement decreased to approximately 7% at x = 500 and x = 1100. Owing to the existence of two faults in the middle of the model, the linear propagation path of the elastic wave was blocked, resulting in complex attenuation characteristics within the range of $0<x<400$ m at the same elevation of the coal seam, and the peak displacement in the fault was significantly lower than that in the adjacent area.

(3) At the same horizontal position (x = 800 m), the displacement attenuation coefficient had a roughly normal distribution. The attenuation coefficient fluctuated at x = 150, 250, 400, and 550 m. The above positions correspond to the interfaces of the rock strata. The different wave velocities of the rock strata on both sides weaken the transmission of the elastic waves. The results show that the attenuation effect of the elastic wave displacement is dominated by long-distance propagation in the strata, and the attenuation of the displacement at the interface is not obvious.

4.2 Stress attenuation law

The stress attenuation is quantitatively expressed by the stress attenuation coefficient, as shown in Eq. (10)

$$\gamma_{\sigma i} = \frac{\sigma_i}{\sigma_s} \tag{10}$$

where $\gamma_{\sigma i}$ is the stress attenuation coefficient at point i, σ_i the principal stress value at point i, and σ_s the principal stress value at the source.

Fig. 9 shows the distribution of the principal stress attenuation coefficients of the grid points in the model. Fig. 10 shows the distribution curve of the principal stress attenuation coefficient on the lines x = 800 m, z = 580 m and z = 650 m. The distribution of the stress attenuation coefficient is similar to that of the displacement attenuation coefficient. As shown in Figs. 9–10.

(1) At z = 580 m and x = 800 m, the stress attenuation coefficient near the source had a roughly normal distribution.

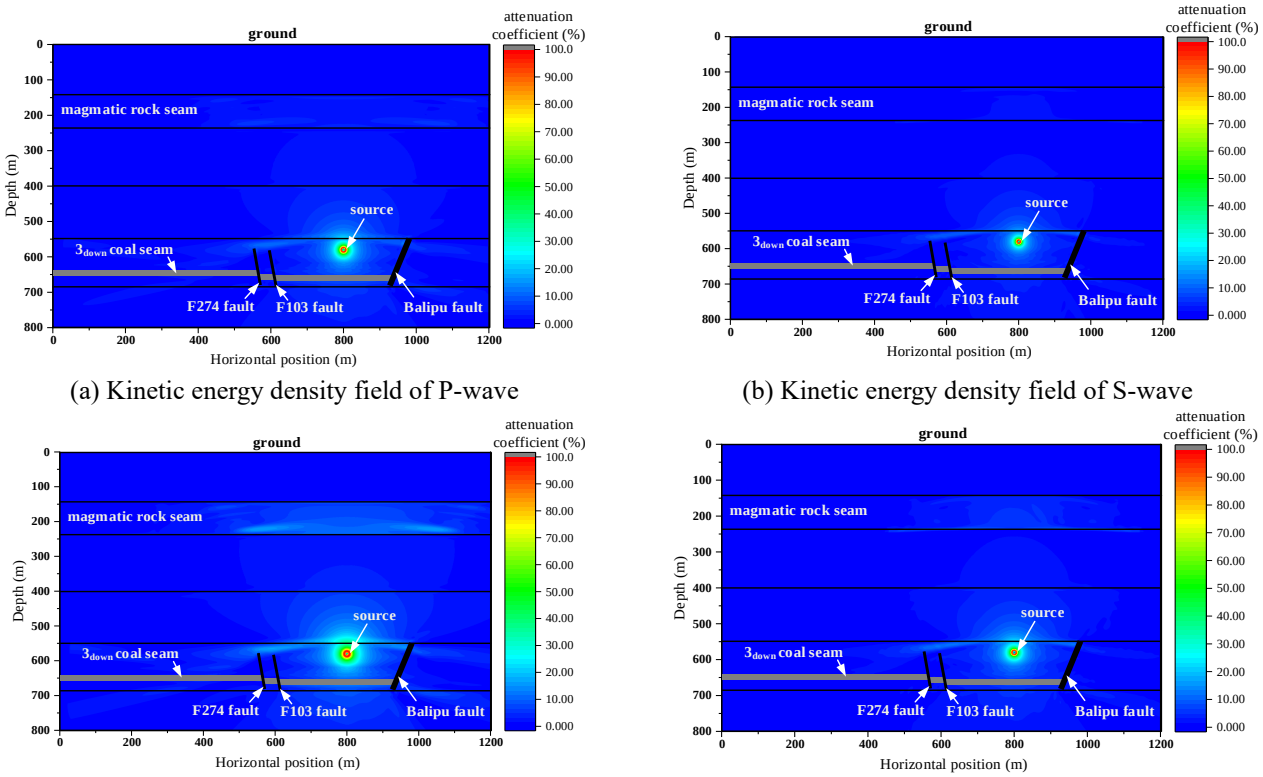

(a) Kinetic energy density field of P-wave

(b) Kinetic energy density field of S-wave

(c) Energy flux field of P-wave

(d) Energy flux field of S-wave

Fig.11 Energy attenuation coefficient distribution cloud map

The stress of the elastic wave emitted by the source decreased rapidly on both sides, and the attenuation coefficient within the 200 m range decreases rapidly to less than 20%. The attenuation coefficient outside the 200 m range has obvious segmental characteristics. This segmented feature was caused by three faults in the horizontal direction and the interface of the strata in the vertical direction. Compared with the displacement attenuation coefficient, the stress attenuation coefficient was more significantly affected by the interface.

(2) After the elastic wave propagated to the coal seam, the peak stress attenuation was less than 25% of the source. The attenuation coefficient within 300 m in the coal seam directly below the source had a roughly linear distribution. At x = 580, 620, and 950 m, there were three obvious drops in the attenuation coefficient. The results show that stress propagation in the horizontal direction is hindered by the fault, and the stress inside the fault is significantly lower than that in the surrounding rock mass. Simultaneously, abnormally high values appear on both sides of the fault, indicating that there is a certain degree of stress concentration around the fault during the elastic wave propagation process.

(3) In both the horizontal and vertical lines, the attenuation coefficient of the P-wave was smaller than that of the S-wave. This shows that the attenuation effect of the additional stress of the P-wave is more obvious than that of the S-wave, owing to the attenuation of the long-distance propagation and scattering of the interface.

4.3 Energy attenuation law

Both the kinetic energy density and energy flux density reflect the intensity of the elastic wave energy that reaches the target region. Therefore, energy attenuation can be represented by the energy density attenuation coefficient, as shown in Eq. (11)

$$\gamma_{Ui} = \frac{U_i}{U_s} \tag{11}$$

where γ_{Ui} is the attenuation coefficient of the energy density at point i, U_i the energy density at point i, and U_s the energy density at the source.

Fig. 11 shows the attenuation coefficient distributions of the kinetic energy density and energy flux density of the grid points in the model. Fig. 12 shows the distribution curve of the energy density attenuation coefficient of the measurement line x = 800 m, z = 580 m, z = 650 m, as shown in Figs. 11 and 12.

(1) Energy attenuation was more evident than displacement attenuation and stress attenuation. In the two measuring lines z = 580 m and x = 800 m, the energy density at a position 200 m away from the source decayed to less than 5% of the source, and the energy density attenuation coefficient at the boundary of the model was only 1%.

(2) After the elastic wave propagated to the coal seam (z = 650 m), the energy density decayed to less than 9% of the source. There are three obvious attenuation coefficient drops at x = 580, 620, and 950 m, indicating that the

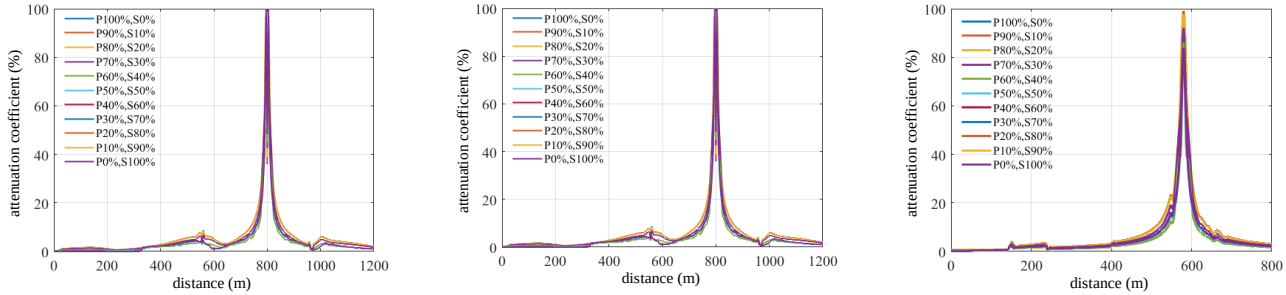

(a) z = 580 (b) z = 650 (c) x = 800

Fig. 12 Energy attenuation coefficient evolution curve

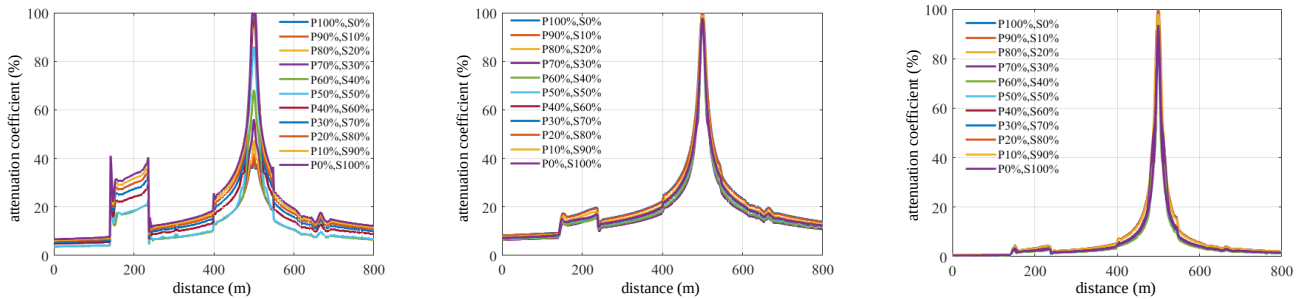

(a) Attenuation coefficient of principal stress (b) Attenuation coefficient of displacement (c) Attenuation coefficient of Kinetic energy density

Fig. 13 Attenuation coefficient evolution curve of x = 800 (focal depth 500 m)

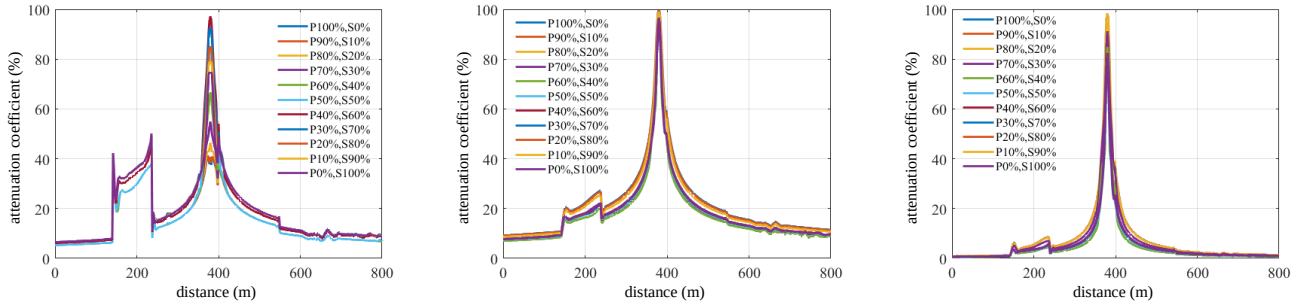

(a) Attenuation coefficient of principal stress (b) Attenuation coefficient of displacement (c) Attenuation coefficient of Kinetic energy density

Fig. 14 Attenuation coefficient evolution curve of x = 800 (focal depth 380 m)

horizontal propagation of energy is hindered by the fault. At the same time, relatively obvious abnormally high values appear on both sides of the fault, indicating that the elastic wave scattering process near the fault occurred at the same time as the subsequent wave field superposition, resulting in a certain degree of high-energy density area around the fault.

5. Discussion

5.1 Influence of different seismic source locations

The seismic source is located at different locations in the stratum, which may affect the propagation attenuation process of elastic waves; this is the focus of this study. To study this problem, two other numerical models with different seismic source locations were established to keep the formation wave velocity field model unchanged. The focal coordinates are (800, 380) and (800, 500), and the propagation attenuation law of the elastic wave generated when the rock stratum is fractured at these two locations is simulated. Figs. 13 and 14 shows the evolution curves of the attenuation coefficients of the two models at x = 800 m. As shown in the figure, when the source was in different layers, the attenuation law of each wave field parameter in the vertical direction was similar to a certain extent. At the same position 100 m away from the source, the principal stress and displacement both decay to approximately 20%, and the kinetic energy density to approximately 8%. This indicates that when the source is located in different strata, the elastic wave exhibits a similar attenuation law and is highly correlated with the propagation distance. This makes the quantitative characterization of the wave-field parameter attenuation feasible.

5.2 Quantitative characterization of elastic wave energy transfer

When an elastic wave from the source propagates to any location in the stratum, the amount of energy it has is a common concern in this type of research. To study the relationship between the elastic wave energy and propagation distance, the evolution law of the attenuation coefficient of the source energy in the vertical direction was analyzed. In the process of analysis, the energy attenuation curve transmitted from the source with coordinates (800, 380) to the rock layer below was fitted, as shown in Fig. 15.

After asymptotically exponential fitting the energy attenuation curve, the energy distance attenuation equation of the elastic wave can be written as follows

$$\gamma_E = 2.6 + 91.5 \times 0.91^x \quad (12)$$

The result of Eq. (12) can be used as an equation to characterize the distance attenuation of the elastic wave energy released by the roof rupture source.

6. Conclusions

The propagation attenuation law of elastic waves generated by rock mass fractures in strata is of great significance in explaining engineering problems, such as rock bursts. In this study, a wave velocity model was established based on the actual stratum conditions of the Jining No.2 coal mine in China. The propagation process of different types of elastic waves is simulated using the elastic wave equation and finite difference method. The attenuation coefficients of various elastic wave parameters propagating at different positions were calculated. The main conclusions of the study are as follows:

- The propagation characteristics of S-waves and P-waves in strata are similar to a certain extent, and the wave pattern conversion occurs at the interface of the strata with rapid attenuation with distance. The magma layer becomes a "waveguide layer," which plays a role in channeling and reflecting the elastic wave propagation, leading to the occurrence of low-energy aftershocks in the coal seam.
- Only part of the elastic wave generated by the fracture of the siltstone layer in the roof of the 3down coal seam in the Jining No. 2 coal mine can propagate to the coal seam, in which the peak displacement attenuation is less than 28% of the source, the stress attenuation less than 25% of the source, and the energy density attenuation less than 9% of the source. There are stress concentration and high energy density areas around the fault.
- The attenuation of elastic wave energy is highly correlated with the propagation distance. Based on the simulation results, an attenuation equation of the elastic wave energy with distance was established, and the attenuation equation was in the form of an exponential function.

Acknowledgments

The research described in this paper was financially supported by National Natural Science Foundation of China (No.52374097, No.52304095), and Shandong Provincial Natural Science Foundation (No.ZR2024QE108).

References

Babanouri, N. and Fattahi, H. (2018), "Evaluating orthotropic continuum analysis of stress wave propagation through a jointed rock mass", *Bull. Eng. Geol. Environ.*, **77**, 725-733. https://doi.org/10.1007/s10064-016-0989-9.

Berjamin, H., Lombard, B., Chiavassa, G. and Favrie, N. (2018), "Modeling longitudinal wave propagation in nonlinear viscoelastic solids with softening", *Int. J. Solids Struct.*, **141-142**, 35-44. https://doi.org/10.1016/j.ijsolstr.2018.02.009.

Cheng, S.J., Mao, W.J., Zhang, Q.C. and Xu, Q.R. (2021), "Wave propagation in the poro-viscoelastic orthorhombic two-phase media: plane-wave theory and wavefield simulation", *Geophys. J. Int.*, **227**(1), 99-122. https://doi.org/10.1093/gji/ggab213.

Chong, S.H., Kim, J.W., Cho, G.C. and Song, K.I. (2020), "Preliminary numerical study on long-wavelength wave propagation in a jointed rock mass", *Geomech. Eng.*, **21**(3), 227-236. https://doi.org/10.12989/gae.2020.21.3.227.

Christensen, N.I. (1971), "Shear wave propagation in rocks", *Nature*, https://doi.org/10.1038/229549b0.

Czarny, R., Malinowski, M., Chamarczuk, M., Cwiekala, M., Olechowski, S., Isakow, Z. and Sierodzki, P. (2021), "Dispersive seismic waves in a coal seam around the roadway in the presence of excavation damaged zone", *Int. J. Rock Mech. Eng.*, **148**, 104937. https://doi.org/10.1016/j.ijrmms.2021.104937.

Fan, L.F., Yi, X.W. and Ma, G.W. (2013), "Numerical manifold method (nmm) simulation of stress wave propagation through fractured rock mass", *Int. J. Appl. Mech.*, **5**(2), 1350022. https://doi.org/10.1142/S1758825113500221.

Fan, Y., Cui, X.Z., Leng, Z.D., Zheng, J.W., Wang, F. and Xu, X.L. (2021), "Rockburst prediction from the perspective of energy release: A case study of a diversion tunnel at Jinping II hydropower station", *Front. Earth Sci.*, **9**, https://doi.org/10.3389/feart.2021.711706.

Fu, L.Y., Fu, B.Y., Sun, W.J. Han, T.C, and Liu, J.L. (2020), "Elastic wave propagation and scattering in prestressed porous rocks", *Sci. China Earth Sci.*, **63**, 1309-1329. https://doi.org/10.1007/s11430-019-9615-3.

Gallagher, A., Fortin, J. and Borgomano, J. (2022), "Seismic dispersion and attenuation in fractured fluid-saturated porous rocks: An experimental study with an analytic and computational comparison", *Rock Mech. Rock Eng.*, **55**, 4423-4440. https://doi.org/10.1007/s00603-022-02875-y.

Gegenhuber, N. (2016), "Interpretation of elastic properties for magmatic and metamorphic rock types", *Int. J. Rock Mech. Min. Sci.*, **88**, 44-48. https://doi.org/10.1016/j.ijrmms.2016.07.007.

Guo, W.Y., Zhang, D.X., Zhao, T.B., Li, Y.R., Zhao, Y.Q., Wang, C.W. and Wu, W.B. (2022), "Influence of rock strength on the mechanical characteristics and energy evolution law of gypsum-rock combination specimen under cyclic loading-unloading condition", *Int J Geomech.*, **22**(5), https://doi.org/10.1061/(ASCE)GM.1943-5622.0002276.

Han, L. and Dai, L.M. (2018), "Spherical wave attenuation under multiple energy source in viscous fluid-saturated elastic porous media", *J. Pet. Sci. Eng.*, **169**, 15-23. https://doi.org/10.1016/j.petrol.2018.05.024.

He, J., Dou, L.M., Mu, Z.L., Cao, A.Y. and Gong, S.Y. (2016),

"Numerical simulation study on hard-thick roof inducing rock burst in coal mine", *J. Cent. South Univ.*, **23**, 2314-2320. https://doi.org/10.1007/s11771-016-3289-4.

Huang, X.G., Greenhalgh, S., Han, L. and Liu, X. (2022), "Generalised effective biot theory and seismic wave propagation in anisotropic, poroviscoelastic media", *J. Geophys. Res. Solid Earth*, **127**(3), https://doi.org/10.1029/2021JB023590.

Lak, M. Marji, M.F., Bafghi, A.Y. and Abdollahipour, A. (2018), "Analytical and numerical modeling of rock blasting operations using a two-dimensional elasto-dynamic Green's function", *Int. J. Rock Mech. Min. Sci.*, **114**, 208-217. https://doi.org/10.1016/j.ijrmms.2018.12.022.

Lak, M., Marji, M.F., Bafghi, A.Y. and Abdollahipour, A. (2019), "A coupled finite difference-boundary element method for modeling the propagation of explosion-induced radial cracks around a well bore", *J. Nat. Gas Sci. Eng.*, **64**, 41-51. https://doi.org/10.1016/j.jngse.2019.01.019.

Lei, Q.H. and Sornette, D. (2021), "Transport and localization of elastic waves in two-dimensional fractured media: Consequences on scattering attenuation", *J. Geophys. Res. Solid Earth*, **126**(6), https://doi.org/10.1029/2020JB021178.

Li, D., Zhang, J.F., Wang, C.W. and Jiang, F.X. (2019), "Propagation patterns of microseismic waves in rock strata during mining: An experimental study", *Int. J. Miner. Metall. Mater.*, **26**, 531-537. https://doi.org/10.1007/s12613-019-1761-5.

Li, X.B. and Tao, M. (2015), "The influence of initial stress on wave propagation and dynamic elastic coefficients", *Geomech. Eng.*, **8**(3), 377-390. https://doi.org/10.12989/gae.2015.8.3.377.

Perino, A., Zhu, JB., Li, J.C., Barla, G. and Zhao, J. (2010), "Theoretical methods for wave propagation across jointed rock masses", *Rock Mech. Rock Eng.*, **43**, 799-809. https://doi.org/10.1007/s00603-010-0114-5.

Rioyos-Romero, R., De Basabe, J.D., Solorza-Calderon, S., Gonzalez-Escobar, M. and Gross, M. (2022), "Comparison of wave-propagation simulations in fractured domains using discrete fractures and equivalent media", *Geophys. J. Int.*, **230**(1), 427-447.https://doi.org/10.1093/gji/ggac014.

Sebastian, R. and Sitharam, T.G. (2018), "Resonant column tests and nonlinear elasticity in simulated rocks", *Rock Mech. Rock Eng.*, https://doi.org/10.1007/s00603-017-1308-x.

Shen, H.M., Li, X.Y. and Li, Q. (2022), "Influence of the microstructure on stress-dependent P-wave anisotropy in sandstone", *Geophys. J. Int.*, **228**(2), 876-892. https://doi.org/10.1093/gji/ggab383.

Tao, M., Chen, Z.H., Li, X.B., Zhao, H.T. and Yin, T.B. (2016), "Theoretical and numerical analysis of the influence of initial stress gradient on wave propagations", *Geomech. Eng.*, **10**(3), 285-296. https://doi.org/10.12989/gae.2016.10.3.285.

Zeng, C., Zhao, C.F. and Zeighami, F. (2022), "Seismic surface wave attenuation by resonant metasurfaces on stratified soil", *Earthq. Eng. Struct. D.*, **51**, 1201-1223. https://doi.org/10.1002/eqe.3611.

Zhao, T.B., Guo, W.Y., Lu, C.P. and Zhao, G.M. (2016), "Failure characteristics of combined coal-rock with different interfacial angles", *Geomech. Eng.*, **11**(3), 345-359. https://doi.org/10.12989/gae.2016.11.3.345.

Zhao, T.B., Guo, W.Y., Tan, Y.L., Yin, Y.C., Cai, L.S. and Pan, J.F. (2018), "Case studies of rock bursts under complicated geological conditions during multi-seam mining at a depth of 800 m", *Rock Mech. Rock Eng.*, **51**, 1539-1564. https://doi.org/10.1007/s00603-018-1411-7.

Zhao, T.B., Zhang, W., Gu, S.T., Lv, Y.W. and Li, Z.H. (2020), "Study on fracture mechanics of granite based on digital speckle correlation method", *Int. J. Solids Struct.*, **193-194**, 192-199. https://doi.org/10.3969/j.issn.1673-3193.2018.05.001.

Zhu, J.B., Ren, M. and Liao, Z.Y. (2020), "Wave propagation and diffraction through non-persistent rock joints: An analytical and numerical study", *Int. J. Rock Mech. Min.*, **132**, 104362. https://doi.org/10.1016/j.ijrmms.2020.104362.

Zhu, J.B., Zhai, T.Q., Liao, Z.Y., Yang, S.Q., Liu, X.L. and Zhou, T. (2020), "Low-amplitude wave propagation and attenuation through damaged rock and a classification scheme for rock fracturing degree", *Rock Mech. Rock Eng.*, **53**, 3983-4000. https://doi.org/10.1007/s00603-020-02162-8.

CC